Supporting Information

Growth of Mixed-Valence 2D α-MnO_x Nanosheets within Interlayer Spaces of Multilayer Ti_3C_2 as an Efficient Air Cathode for Rechargeable Li-O_2 Batteries

Aqrab ul Ahmad†, William G Morais†, Tauqeer Ahmad, Ihsan Çaha, Isilda Amorim, Siva Sankar, Francis Leonard Deepak*

International Iberian Nanotechnology Laboratory (INL), Avenida Mestre Jose Veiga, Braga 4715-330, Portugal

†authors contributed equally

*email: leonard.francis@inl.int

1. Experimental Section

1.1. Materials and Methods

Reagents: manganese chloride ($MnCl_2 \cdot 4H_2O$ 99%), potassium borate, lithium fluoride powder (LiF), Ti_3AlC_2 MAX phase, N, N-dimethylformamide (DMF 98%), ethanol, hydrochloric acid (HCl 30% diluted), LiTFSI (lithium bis(trifluoromethane)sulfonimide), TEGDME (tetraethylene glycol dimethyl ether) were purchased from Sigma Portugal. Super P carbon (C-NERGY, Nanografi) and polyvinylidene fluoride (PVDF, Nanografi). All chemicals were analytical-grade reagents and used as received.

1.2. Synthesis of $Ti_3C_2T_x$ MXene.

Multilayer $Ti_3C_2T_x$ MXene was produced by selectively etching Ti_3AlC_2 with a LiF/HCl solution. Typically, 1.0 g of LiF was dissolved in 20 mL of 9 M HCl, then 1.0 g of Ti_3AlC_2 was gradually added while stirring. The mixture was kept at 35 °C for 24 hours to remove the Al layer and form $Ti_3C_2T_x$ with -O/-OH/-F terminations. The product was washed repeatedly by centrifugation until the supernatant reached a pH of approximately 6, resulting in multilayer MXene.

1.3. Delamination and In-situ growth of 2D α-MnO_x

To produce delaminated $Ti_3C_2T_x$ and simultaneously induce 2D α-MnO_x formation, 200 mg of etched MXene was dispersed in 20 mL of dimethyl sulfoxide (DMSO) and stirred for 30 minutes. DMSO functions as an intercalation agent, weakening van der Waals forces between layers and facilitating ion penetration. Subsequently, 0.5 mmol of $MnCl_2 \cdot 4H_2O$ was directly added to the MXene-DMSO mixture. Mn^{+2} diffuses into the interlayers via the swollen galleries created by DMSO, forming confined nucleation sites. Shortly after, 10 mL of 1.0 M potassium borate solution was added. The borate ions ($B(OH)_4^-$) create a mildly alkaline environment (pH ≈ 8-9) that promotes the partial oxidation of Mn^{+2} to Mn^{+3}/Mn^{+4}, while also transiently coordinating with Mn to stabilize the edge-sharing MnO_6 octahedra typical of α-MnO_x. The entire reaction mixture was heated at 40 °C for 12 hours. This moderate temperature promotes interlayer diffusion and gradual redox conversion while preventing bulk MnO_x precipitation. Confinement within MXene interlayers results in the formation of 2D α-MnO_x nanosheets. In this mild redox process, synergistic oxidation occurs due to (i) borate-buffered alkaline conditions, (ii) oxygen-containing MXene surface groups (-O and -OH), and (iii)

DMSO-limited oxidative ability at higher temperatures. Consequently, Mn^{+2} is slowly oxidized to a complex mixture of Mn^{+4}, Mn^{+3}, and Mn^{+2}, with the confined $Ti_3C_2T_x$ layers stabilizing this distribution. After 12 hours, the solid product was collected by centrifugation, washed with water and ethanol to remove unreacted Mn^{2+}/borate/DMSO, and then dried in a vacuum oven at 60 °C. The resulting powder is labelled as 2D α-MnO_x@M-Ti_3C_2.

To further verify the spatial distribution of MnO_x within the multilayered Ti_3C_2 MXene structure, a cross-sectional lamella was prepared by FIB-SEM and analyzed by SEM-EDS line profiling (Fig. S1). The lamella, extracted perpendicular to the MXene basal planes, enables direct probing across the stacked layers. The corresponding EDS line profile reveals a clear and continuous Mn signal that spatially correlates with the Ti signal throughout the multilayer region, rather than being confined to the outer surface.

Importantly, the Mn intensity exhibits periodic fluctuations that follow the layered morphology of the Ti_3C_2 scaffold, indicating that Mn-containing species are distributed within the interlayer galleries rather than forming isolated surface aggregates. The absence of a sharp Mn enrichment exclusively at the outer edges further rules out dominant surface decoration or particle segregation. Instead, the co-localization of Mn and Ti signals across the lamella thickness provides strong evidence that MnO_x is intercalated and confined within the MXene interlayers.

These results directly support the proposed in situ growth mechanism, where Mn^{2+} ions intercalate into the swollen MXene galleries during DMSO-assisted delamination and subsequently undergo confined oxidation to form 2D MnO_x nanosheets within the interlayer spaces. This nanoscale confinement explains the layered distribution observed in the EDS profile and corroborates the structural model proposed in the main manuscript.

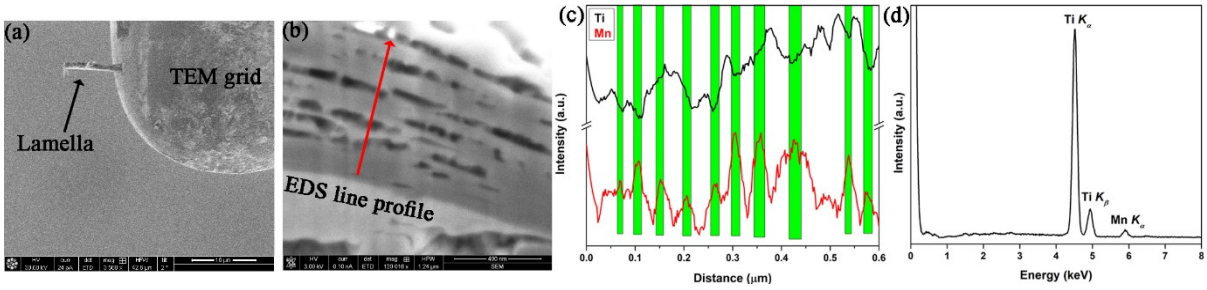

Figure S1. (a) SEM image of the MXene lamella on TEM grid. (b) SEM image with EDS line scan path (red arrow). (c) EDS line profile showing Ti (black) and Mn (red) distribution across the layers (green shaded regions). The correlated signals confirm MnO_x distribution within the interlayers. (d) EDS spectrum showing Ti and Mn peaks.

1.4. Air cathode preparation and cell assembly

The electrodes were prepared by mixing the active material with Super P carbon (C-NERGY, Nanografi) and polyvinylidene fluoride (PVDF, Nanografi) in a weight ratio of 70:20:10 using N-methyl-2-pyrrolidone (NMP, Merck) as the solvent to form a homogeneous slurry. The resulting slurry was uniformly coated onto carbon paper (microporous layer with PTFE, Quintech) and subsequently dried under vacuum at 80 °C overnight. The dried electrodes were then punched into 12 mm diameter disks, with the mass of the active material (2D α-MnO_x@M-Ti_3C_2) controlled to achieve a loading of approximately 1.4 mg cm^{-2}.

CR2032-type coin cells with meshed positive cases were assembled using the prepared air cathode and a lithium metal disk as the counter/reference electrode. A volume of 150 µL of 1 M LiTFSI

(lithium bis(trifluoromethane)sulfonimide) dissolved in TEGDME (tetraethylene glycol dimethyl ether) was used as the electrolyte, and a glass fiber separator (Whatman GF/F) was employed. All cell assembly procedures were carried out in an argon-filled glove box with H_2O and O_2 levels maintained below 0.5 ppm.

1.5. Electrochemical Measurements

Electrochemical measurements were performed using a WBCS3000 battery test system (WonATech). Galvanostatic charge/discharge tests were conducted within a voltage window of 2.0 – 4.3 V (vs. Li/Li^+) at current densities of 100, 200, and 500 mA g^{-1}at room temperature. Cycling stability was evaluated under a fixed discharge capacity limit of 500 mAh g^{-1}.

1.6. Structural Characterizations

Crystallographic features, including crystalline structure and phase identification, were examined using X-ray Diffraction (XRD) with a LabX XRD-6100 diffractometer. Morphological features were captured using a Zeiss Sigma 500 scanning electron microscope (SEM). Element distribution was analyzed in conjunction with energy-dispersive X-ray spectroscopy (EDS). Chemical vibrations were evaluated with a Horiba LabRAM HR Evolution confocal Raman spectrometer equipped with a 532 nm laser. Surface chemical states and elemental composition were analyzed by X-ray photoelectron

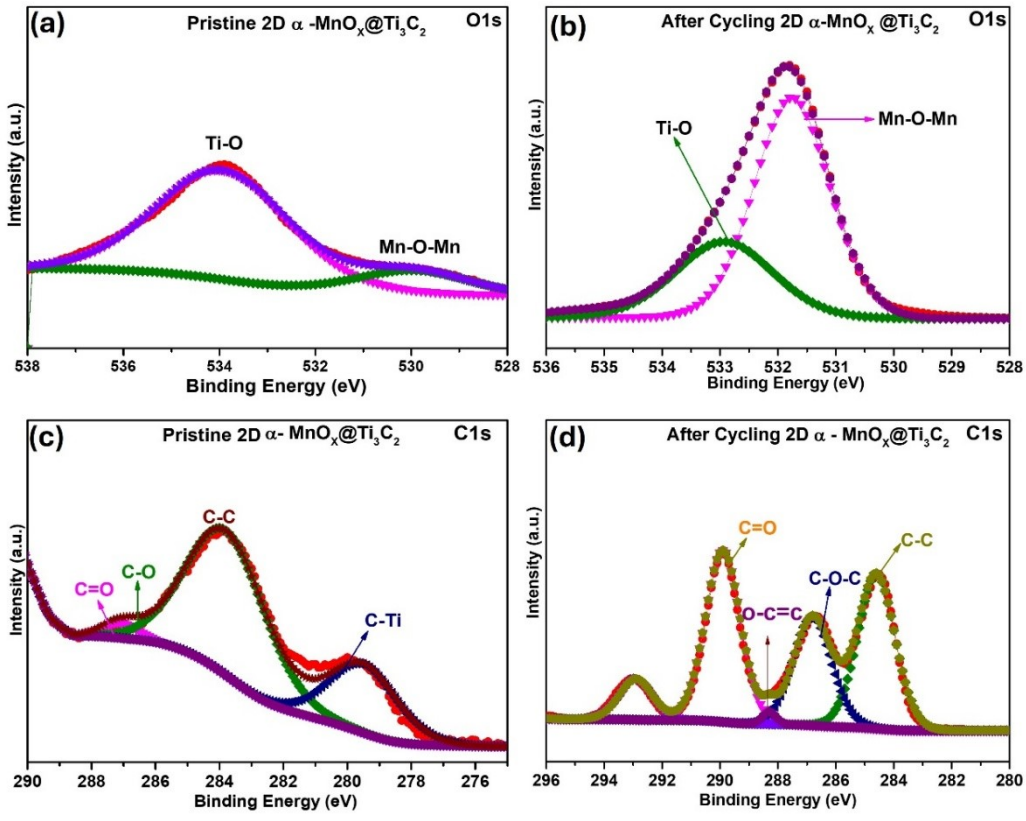

spectroscopy (XPS) using an ESCALAB Xi^+ system.

Figure S2: High-resolution XPS spectra of 2D α-MnO_x@M-Ti_3C_2 before and after cycling in a Li-O_2 battery: **(a)** O1s spectrum of the pristine electrode, **(b)** O1s spectrum after cycling, **(c)** C1s spectrum

of the pristine electrode, and **(d)** C1s spectrum after cycling, showing changes in metal–oxygen bonding and the formation of oxygen-containing carbon species during electrochemical operation.

In the pristine state, the O 1s spectrum (**Fig S1 a**) exhibits characteristic peaks corresponding to Ti–O and Mn–O–Mn, confirming the successful integration of α-MnO_2 with the M-Ti_3C_2 MXene framework. After cycling (**Fig S1 b**), the increased intensity of the Mn–O–Mn component indicates enhanced involvement of Mn-based oxide species during the oxygen reduction and evolution reactions (ORR/OER), highlighting the catalytic role of α-MnO_x in facilitating Li-O_2 electrochemistry. The C1s spectra further elucidates interfacial changes occurring during battery operation. The pristine electrode (**Fig S1 c**) shows typical MXene-related bonding states, including C–C, C–O, C=O, and C–Ti, confirming the preserved carbide structure of M-Ti_3C_2. After cycling (**Fig S1 d**), new and intensified oxygenated carbon species such as C–O–C and O–C=O are observed, which are attributed to electrolyte decomposition and formation of discharge by-products. These changes indicate strong interfacial interactions between the electrode surface and reaction intermediates during repeated Li-O_2 cycling

Figure S3. EDS spectra collected from different regions of the α-2D MnO_x@M-Ti_3C_2 electrode after 54 Li-O_2 battery cycles, showing the presence of C, Ti, Mn, and O with spatial variations in elemental intensities due to non-uniform discharge product deposition and electrolyte/binder decomposition.

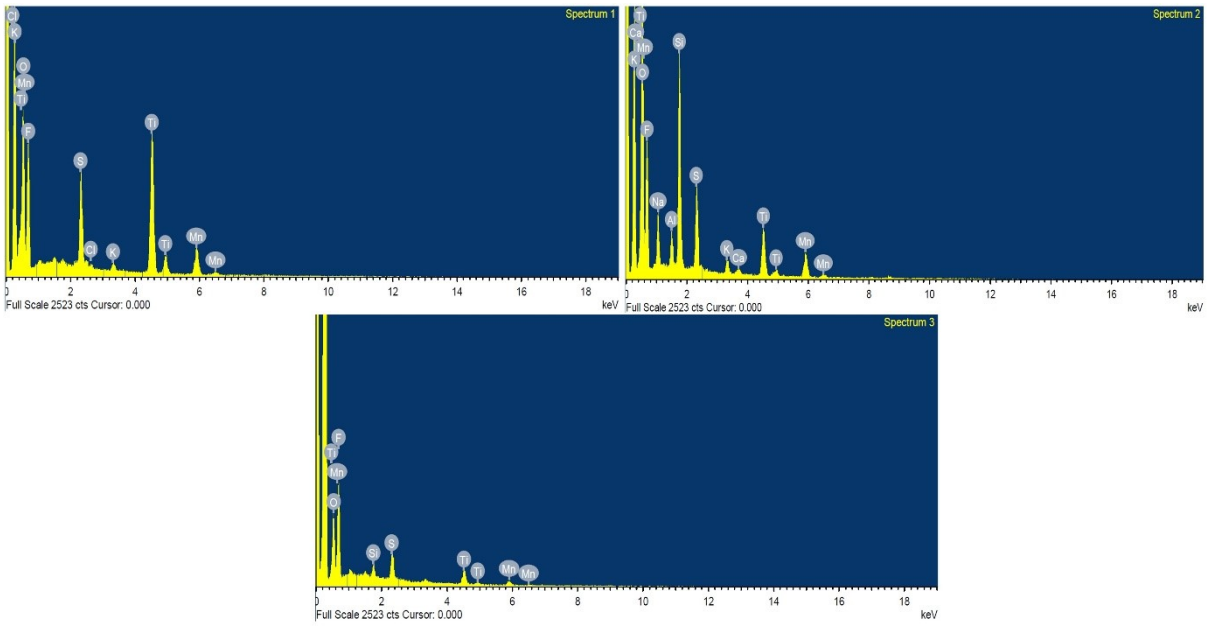

EDS spectra collected from different areas of the α-2D MnO_x@M-Ti_3C_2 electrode after 54 Li-O_2 battery cycles show consistent signals of C, Ti, Mn, and O, confirming the structural retention of the MnO_x catalyst anchored on the Ti_3C_2 MXene framework. However, noticeable variations in peak intensities among the spectra indicate surface heterogeneity after prolonged cycling. Regions with stronger Ti and Mn signals suggest well-exposed and electrically connected MnO_x active sites, while areas with higher O and C intensities and detectable F- and S-containing species point to the accumulation of discharge products and electrolyte/binder decomposition residues. These results imply non-uniform deposition of Li-O_2 reaction products, leading to partial surface passivation in some regions, which is consistent with the gradual performance degradation observed during extended cycling.

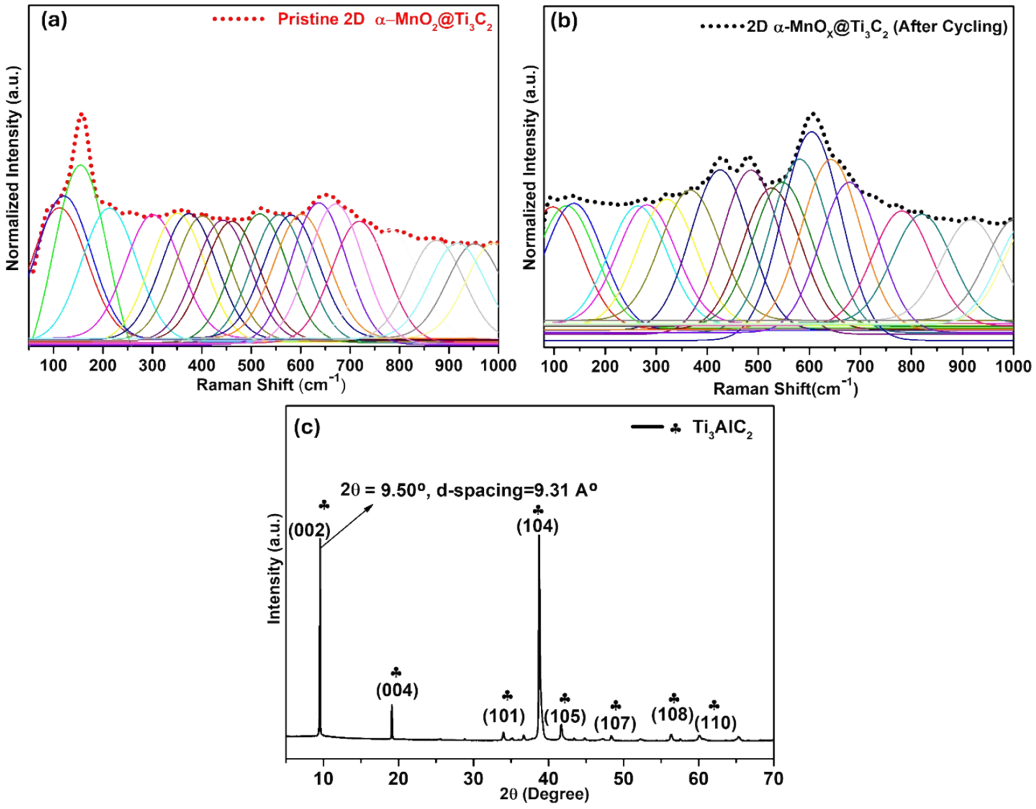

Figure S4. (a-b)Peak deconvolution analysis of the Raman spectra before and after cycling of 2D α-MnO_x@Ti_3C_2 and (c) X-ray diffraction (XRD) patterns of MAX Phase.

Table S1. Summary and comparison of Li-O_2 battery performance with MnO_2-based electrocatalysts. *mA g^{-1}

Catalyst	Maximum Capacity	Rate performance	Cycling performance	Ref

	Capacity (mA h g^{-1})	Current (mA cm^{-2})	Capacity (mA h g^{-1})	Current (mA cm^{-2})	cycles	Current (mA cm^{-2})	Capacity (mA h g^{-1})	
α-MnO_2/N-GNF	4706	0.1	3260	0.2	50	-	500	[1]
Porous ε-MnO_2	5700	100*	3400	800	190	500	800	[2]
α-MnO_2/CRT	4675	400*	-	-	303	800	1000	[3]
3D α-MnO_2	8583	100*	6311	300	170	200	1000	[4]
γ-MnO_2/G	11235	75*	6023	300	30	215	1500	[5]
α-MnO_2/GN	2500	50*	1632	300	47	100	1000	[6]
α-MnO_2/Co_3O_4	4850	100*	3401	618	50	103	1030	[7]
3D-G/δ-MnO_2	3660	48*	770	387	132	193	1000	[8]
α-MnO_2	6225	0.1	-	-	35	-	800	[9]
α-MnO_2/C	1400	100	-	-	40	100	500	[10]
α-MnO_2 nanowires	3000	500	-	-	10	-	408	[11]
MnO_2-CNTs hybrid	2247	-	2250	0.025	6	-	557	[12]
carbon supported-MnO_2 hybrid	4750	-	-	-	50	-	3450	[13]
MnO_2 nanotubes	-	-	-	-	30	-	250	[14]
2D- α-MnOx@Ti_3C_2	**14,377**	**100***	**11,242**	**300**	**54**	**500**	**500**	**This work**

Table S2: Comparison pure Mn^{3+}, pure Mn^{4+} and mixed valence catalytic activity.

Catalyst	ORR onset	OER onset	ΔE (ORR–OER, V)	Reference

α-Mn_2O_2 (pure 3+)	0.82 (V vs. RHE)	2.2 (V vs. RHE)	1.38	Single-Atom Ni Anchored on α-MnO2 Nanorods as an Electrocatalyst for the Oxygen Evolution and Oxygen Reduction Reactions | ACS Applied Nano Materials
α-Mn_2O_3 (pure 4+)	0.40 (V vs. RHE)	2.39 (V vs. RHE)	1.99	**https://doi.org/10.1039/C6DT03158G** and Manganese dissolution in alkaline medium with and without concurrent oxygen evolution in LiMn2O4
Mixed Mn^{3+}/Mn^{4+}	**2.75 (V vs. Li/Li^+)**	**3.60 (V vs. Li/Li^+)**	**0.85***	**This work**

* at 100 mA g^{-1}.

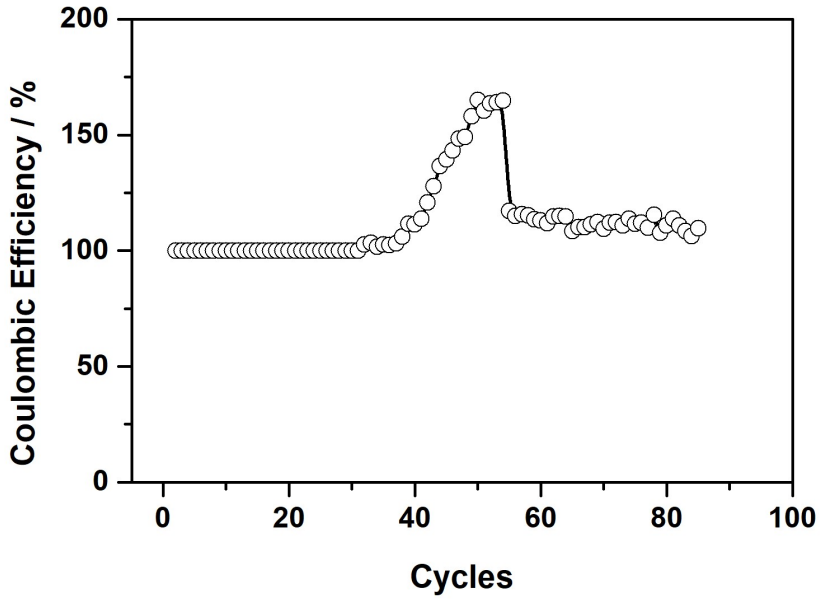

Figure S5. Coulombic efficiency of the LAB cell cycled at 500 mA g^{-1} with discharge limit of 500 mAh g^{-1}.

References:

1 A. Zahoor, M. Christy, H. Jang, K. S. Nahm and Y. S. Lee, *Electrochim. Acta*, 2015, **157**, 299–306.

2 X. Hu, F. Cheng, X. Han, T. Zhang and J. Chen, *Small*, 2015, **11**, 809–813.

3 F. Tu, Q. Wang, J. Xie, G. Cao, S. Zhang, J. Wang, S. X. Mao, X. Zhao and H. Y. Yang, *Energy Storage Mater.*, 2017, **6**, 164–170.

4 R. Bi, G. Liu, C. Zeng, X. Wang, L. Zhang and S. Z. Qiao, *Small*, 2019, **15**, 1–7.

5 Y. Yang, M. Shi, Y.-S. Li and Z.-W. Fu, *J. Electrochem. Soc.*, 2012, **159**, A1917–A1921.

6 Y. Cao, M. Sen Zheng, S. Cai, X. Lin, C. Yang, W. Hu and Q. F. Dong, *J. Mater. Chem. A*, 2014, **2**, 18736–18741.

7 P. Zhang, S. Zhang, M. He, J. Lang, A. Ren, S. Xu and X. Yan, *Adv. Sci.*, DOI:10.1002/advs.201700172.

8 S. Liu, Y. Zhu, J. Xie, Y. Huo, H. Y. Yang, T. Zhu, G. Cao, X. Zhao and S. Zhang, *Adv. Energy Mater.*, 2014, **4**, 1–9.

9 A. Zahoor, H. S. Jang, J. S. Jeong, M. Christy, Y. J. Hwang and K. S. Nahm, *RSC Adv.*, 2014, **4**, 8973–8977.

10 Y. Qin, J. Lu, P. Du, Z. Chen, Y. Ren, T. Wu, J. T. Miller, J. Wen, D. J. Miller, Z. Zhang and K. Amine, *Energy Environ. Sci.*, 2013, **6**, 519–531.

11 A. Débart, A. J. Paterson, J. Bao and P. G. Bruce, *Angew. Chemie - Int. Ed.*, 2008, **47**, 4521–4524.

12 J. Li, N. Wang, Y. Zhao, Y. Ding and L. Guan, *Electrochem. commun.*, 2011, **13**, 698–700.

13 H. Cheng and K. Scott, *J. Power Sources*, 2010, **195**, 1370–1374.

14 T. T. Truong, Y. Liu, Y. Ren, L. Trahey and Y. Sun, *ACS Nano*, 2012, **6**, 8067–8077.